

Characterization of anisotropic thermal conductivity of suspended nm-thick black phosphorus with frequency-resolved Raman spectroscopy

Tianyu Wang, Meng Han, Ridong Wang, Pengyu Yuan, Shen Xu, and Xinwei Wang

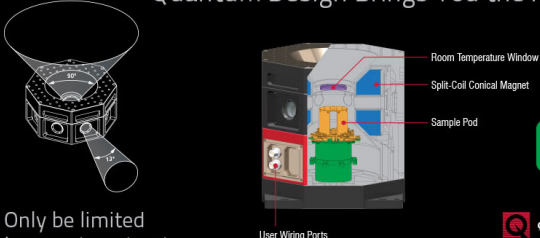
Citation: *Journal of Applied Physics* **123**, 145104 (2018); doi: 10.1063/1.5023800

View online: <https://doi.org/10.1063/1.5023800>

View Table of Contents: <http://aip.scitation.org/toc/jap/123/14>

Published by the *American Institute of Physics*

Quantum Design Brings You the Next Generation Magneto-Optic Cryostat




Only be limited by your imagination...

[Learn More](#)

Quantum Design
qdusa.com/opticool5

8 Optical Access Ports: 7 Side; 1 Top
Temperature Range: 1.7 K to 350 K
7 T Split-Coil Conical Magnet
Low Vibration: <10 nm peak-to-peak
89 mm x 84 mm Sample Volume
Automated Temperature & Magnet Control
Cryogen Free



Characterization of anisotropic thermal conductivity of suspended nm-thick black phosphorus with frequency-resolved Raman spectroscopy

Tianyu Wang,^{1,a)} Meng Han,^{1,a)} Ridong Wang,¹ Pengyu Yuan,¹ Shen Xu,^{2,b)} and Xinwei Wang^{1,b)}

¹Department of Mechanical Engineering, Iowa State University, 2025 Black Engineering Building, Ames, Iowa 50010, USA

²Automotive Engineering College, Shanghai University of Engineering Science, 333 Longteng Road, Shanghai, People's Republic of China

(Received 28 January 2018; accepted 25 March 2018; published online 10 April 2018)

Frequency-resolved Raman spectroscopy (FR-Raman) is a new technique for nondestructive thermal characterization. Here, we apply this new technique to measure the anisotropic thermal conductivity of suspended nm-thick black phosphorus samples without the need of optical absorption and temperature coefficient. Four samples with thicknesses between 99.8 and 157.6 nm are studied. Based on steady state laser heating and Raman measurement of samples with a specifically designed thermal transport path, the thermal conductivity ratio (κ_{ZZ}/κ_{AC}) is determined to be 1.86–3.06. Based on the FR-Raman measurements, the armchair thermal conductivity is measured as 14–22 W m⁻¹ K⁻¹, while the zigzag thermal conductivity is 40–63 W m⁻¹ K⁻¹. FR-Raman has great potential for studying the thermal properties of various nanomaterials. This study significantly advances our understanding of thermal transport in black phosphorus and facilitates the application of black phosphorus in novel devices. *Published by AIP Publishing.*

<https://doi.org/10.1063/1.5023800>

I. INTRODUCTION

In recent years, black phosphorus (BP) has attracted worldwide research interest as a promising layered material for electronic, optical and optoelectronic applications. Compared with other two-dimensional materials, BP possesses many extraordinary properties, such as high carrier mobility (~ 1000 cm² V⁻¹ s⁻¹ in field-effect transistors) and thickness-dependent direct bandgap, which varies from 0.3 eV (bulk) to 1.4 eV (monolayer).^{1–4} Most intriguingly, with a honeycomb layered structure, BP has unique anisotropy in its electrical,^{2–5} optical,^{6–8} mechanical,^{9–12} and thermal^{13–18} properties. Such anisotropy is commonly described by two high-symmetry lattice directions, the armchair direction and the zigzag direction. These properties make BP an ideal platform for the fundamental study, as well as for designing novel devices. For small-scale BP devices, their performance is not only directly determined by BP's electronic properties, but also relevant to BP's thermal properties, especially the anisotropic thermal conductivity. The study on the anisotropic thermal conductivity of BP is critical for the thermal management and the successful application of BP-based devices.

Compared with extensive investigations on the electronic properties of BP, experimental studies of the anisotropic thermal conductivity of BP are still limited. This is mainly due to technical challenges in sample preparation and experimental measurements. For example, BP is easily oxidized in air by absorbing oxygen molecules and moisture.

Also, with a relatively small lateral size, thin BP is very difficult to handle. Despite these difficulties, Luo *et al.* pioneered measurements of the anisotropic thermal conductivity of few-layered BP samples at room temperature with micro-Raman spectroscopy.¹³ The measured armchair and zigzag thermal conductivities were about 20 and 40 W m⁻¹ K⁻¹, respectively, for BP samples thicker than 15 nm, and they decreased to 10 and 20 W m⁻¹ K⁻¹, respectively, as the BP thickness is reduced to 9.5 nm. Meanwhile, similar results were reported using the micro-bridge technique.¹⁷ Exfoliated BP samples were fabricated into nanoribbons along the armchair and zigzag directions with electron beam lithography (EBL). By bridging BP nanoribbons between two suspended pads, the thickness and temperature dependence of the anisotropic thermal conductivity of BP were investigated. Jang *et al.* measured 138–552 nm thick BP samples with the time-domain thermoreflectance (TDTR) method.¹⁴ These BP samples were protected with a thin AlO_x layer to prevent oxidation. The measured thermal conductivities were 26–34 and 62–86 W m⁻¹ K⁻¹ in armchair and zigzag directions, respectively, at room temperature. Sun *et al.* further improved TDTR measurements by studying bulk BP. It was reported that the armchair and zigzag thermal conductivities were 23–33 and 73–93 W m⁻¹ K⁻¹, respectively.¹⁶ There are other techniques that can be used for studying the anisotropic thermal conductivity of BP, such as the modified laser-flash technique,¹⁹ pulsed laser-assisted thermal relaxation technique,²⁰ transient electro-thermal technique,^{21–24} etc.

As a nondestructive and noncontact technique, micro-Raman spectroscopy offers many compelling advantages over other techniques, such as high spatial resolution, a simple experimental setup, and an easy sample preparation

^{a)}T. Wang and M. Han contributed equally to this work.

^{b)}Authors to whom correspondence should be addressed: xx_xs316@iastate.edu and xwang3@iastate.edu

method.^{25–27} Micro-Raman spectroscopy utilizes a continuous-wave (CW) laser to induce the heating effect and excite Raman scattering simultaneously. The temperature dependence of Raman spectrum makes it possible to probe local temperature changes and determine the thermal properties of a studied system. The successful employment of micro-Raman spectroscopy requires calibrating Raman spectrum with temperature by measuring the temperature coefficient χ , and calculating the absorbed laser power P_0 . However, χ and P_0 are two major sources of measurement errors. To reduce or even eliminate errors induced by χ and P_0 , frequency-resolved Raman spectroscopy (FR-Raman) has been developed in our lab.²⁸ This new technique enables the measurement of thermal properties even without the knowledge of χ and P_0 . It has been successfully applied to measure the thermal diffusivity of a c-Si micro-cantilever.²⁸ In this work, the FR-Raman technique is further developed so that the anisotropic thermal conductivity of suspended BP samples can be measured.

II. PHYSICAL PRINCIPLES OF THE MEASUREMENT

The FR-Raman method utilizes a square-wave modulated laser to induce the heating effect and excite Raman scattering. In each period of a modulated laser, there are a laser-on time τ_h and a laser-off time τ_c (τ_c is always equal to τ_h). Under irradiation of a modulated laser, a sample experiences alternate heating and cooling, and can reach a steady periodic thermal state at last. At a steady periodic thermal state, the temperature rise during τ_h is equal to the temperature drop during τ_c . The average temperature rise $\bar{\theta}$ during τ_h is modulation-frequency (f) dependent. In general, a modulated laser has enhanced heating effect as f decreases. The heating effect of a modulated laser at a very high and a very low f is two extreme cases. At a very high f , temperature variations during τ_h and τ_c are so small that temperature can be regarded as a constant. This state is defined as the “quasi-steady state” with an average temperature rise $\bar{\theta}_{qs}$ during τ_h .

At a very low f , temperature increases from the initial temperature T_0 and converges to its steady state temperature T_s during τ_h , while it decreases from T_s and returns T_0 during the following τ_c . This state is defined as the “steady state” with an average temperature rise $\bar{\theta}_s$ during τ_h ($\bar{\theta}_s$ is equal to $T_s - T_0$). In fact, the thermal response to a low- f modulated laser during τ_h is identical to the thermal response to a continuous-wave laser. From a high f to a low f , the thermal response varies from the “quasi-steady state” to the “steady state” gradually. The corresponding average temperature rise $\bar{\theta}$ increases from $\bar{\theta}_{qs}$ to $\bar{\theta}_s$. Our previous work has rigorously proved that $\bar{\theta}_{qs} = \bar{\theta}_s/2$.²⁸ In addition to the modulation frequency f , $\bar{\theta}$ is also a function of the absorbed laser power and the thermal properties of the studied system. Once $\bar{\theta}$ is normalized by $\bar{\theta}_s$, we have the normalized average temperature rise $\bar{\theta}_{nor}$, which is a dimensionless quantity representing the relative temperature variation. $\bar{\theta}_{nor}$ varies from 1/2 to 1 when f decreases. Such f -dependent variation in $\bar{\theta}_{nor}$ is only determined by the thermal properties of the studied system. In the FR-Raman technique, the temperature dependence of Raman spectrum enables it to monitor the variation of $\bar{\theta}_{nor}$ with f and extract the thermal properties ultimately.

For the anisotropic thermal conductivity of BP, measurements are achieved by suspending a BP sample on a square dent [Fig. 1(a)] in a c-Si substrate. The armchair and zigzag directions of BP are deliberately aligned along an edge of the square dent. This suspending configuration can simplify the thermal transport model for calculating the anisotropic thermal conductivity. The initial suspended sample is called the “as transferred” sample. First, we irradiate the “as transferred” sample with a modulated laser beam and measure its Raman spectra over a wide modulation frequency range [Fig. 1(b)]. The variation of wavenumber against modulation frequency can be obtained from this measurement. Then, the “as transferred” sample [Fig. 1(c)] is irradiated with a CW laser of varying power P and Raman spectra are collected. The power

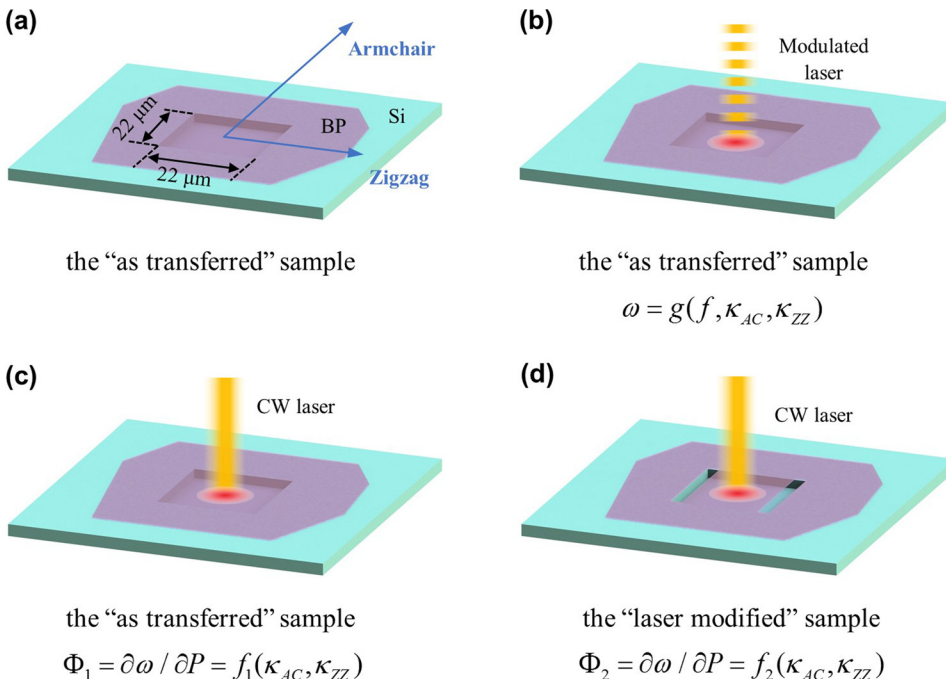


FIG. 1. (a) Schematic of a BP sample suspended on a square dent ($22 \times 22 \times 3 \mu\text{m}^3$). The armchair/zigzag direction is along the edges of the square dent. (b) Irradiation of an “as transferred” suspended BP sample by a modulated laser beam. (c) Irradiation of an “as transferred” suspended BP sample by a CW laser beam. (d) Irradiation of a “laser modified” suspended BP sample by a CW laser beam.

differential of the wavenumber Φ_1 is obtained as $\Phi_1 = \partial\omega/\partial P$. Note that Φ_1 depends on the armchair thermal conductivity κ_{AC} and the zigzag thermal conductivity κ_{ZZ} . Then, we cut two sample's edges along the armchair direction [Fig. 1(d)] to separate them from the substrate. This is achieved by using a high-power CW laser beam. The sample after laser cutting is called the "laser modified" sample. The "laser modified" sample is irradiated with a CW laser of varying power and the counterpart Φ_2 can be obtained. The "laser modified" sample enables the isolation of heat conduction along the armchair direction. Therefore, for this sample, Φ_2 is predominantly determined by κ_{AC} . The thermal conductivity ratio η (κ_{ZZ}/κ_{AC}) can be determined from Φ_2/Φ_1 . The absolute values of κ_{AC} and κ_{ZZ} are extracted from the normalized averaged temperature rise θ_{nor} , which is converted from the wavenumber. Detailed discussions are given in Secs. III–VIII.

III. EXPERIMENTAL SETUP OF FR-RAMAN

The FR-Raman system has an external 532-nm CW laser (Excelsior-532-150-CDRH Spectra-Physics) as an energy source. It is integrated into a confocal Raman system by several mirrors. The CW laser is modulated with a square waveform using an electro-optics modulator (EOM). Driven by a function generator, the EOM can modulate the laser at a frequency as high as 20 MHz. This modulation frequency range is broad enough to induce thermal responses from the "quasi-steady state" to the "steady state". Turning on/off the EOM allows an easy and rapid switching between a modulated laser and a CW laser. During FR-Raman measurements, BP samples are placed in an environmental cell (Linkam Scientific), which can be filled with N_2 gas to prevent the degradation of BP in air.¹⁸ The environmental cell has a circular glass window on its top lid allowing the passing-through of a laser beam. The laser beam is focused by a $20\times$ objective. The spot size is $2\ \mu\text{m}$ at $1/e^2$ of the center intensity. By mounting the environmental cell on a 3D piezo microstage, the laser beam can be focused on the middle of a suspended BP sample precisely. A half-wave plate is applied to adjust laser polarization. A neutral density (ND) filter is utilized to vary the laser power. All Raman spectra are collected in the backscattering configuration. The detailed experimental setup can be found in our previous work.^{18,29}

IV. SUSPENDED BP SAMPLE FABRICATION AND EXPERIMENTAL METHODS

Due to the weak van der Waals force between atomic layers and strong covalent bonds in the layer, a few-layered BP sample can be exfoliated from its bulk counterpart.³⁰ In this work, BP samples are exfoliated from a bulk BP crystal (99.998%, Smart Element) using a modified mechanical exfoliation method.^{31,32} For this modified method, the employment of viscoelastic stamps (PF-20/1.5-X4 Gelfilm from Gelpak) substantially increases the chance of obtaining large and uniform BP samples and reduces sample contamination at the same time. Exfoliated BP samples picked up by viscoelastic stamps are then inspected under an optical microscope. From their color contrast, thicknesses of these

exfoliated BP samples can be estimated roughly. Therefore, candidate BP samples with a large lateral size and a uniform thickness can be identified easily and rapidly. Candidate BP samples on the surface of a viscoelastic stamp can be transferred onto other substrate by simply putting the stamp in gentle contact with the substrate and peeling it slowly with the aid of micro-manipulators. Here, candidate BP samples are transferred and suspended onto square dents ($22 \times 22 \times 3\ \mu\text{m}^3$), which are fabricated on Si wafers with a focused ion beam (FIB). In practice, the alignment of the armchair and zigzag directions along the edges of a square dent is achieved by aligning a naturally formed edge of an exfoliated BP sample along one arbitrary edge of a square dent. Previous research has adequately confirmed that a BP's naturally formed edge is always in the armchair or zigzag direction.^{29,33} Note that we only choose BP samples with at least one naturally formed edge to prepare suspended BP samples.

The suspended BP sample is then loaded into the N_2 -filled environmental cell. The oxidation effect on the suspended BP sample is negligible since the total air-exposure time during sample preparation is typically less than 3 min. Before performing the FR-Raman experiment, we first identify the armchair and zigzag directions of a BP sample with the OT-Raman technique.²⁹ This technique utilizes the anisotropic heating effect of a linearly polarized laser to identify crystalline orientation. This step confirms that the armchair/zigzag direction is in the direction of a BP's naturally formed edge. More importantly, the identification of the armchair and zigzag directions is the prerequisite for fabricating a "laser modified" sample from an "as transferred" sample. Then, we can begin to do the FR-Raman experiment. To keep the consistency of FR-Raman experiments conducted on various BP samples, laser polarization is always aligned along the armchair direction. After the FR-Raman experiment, the sample thickness is determined accurately with an atomic force microscope (AFM).

V. RAMAN MEASUREMENTS AND DATA PROCESSING

We take measurements performed on the 157.6-nm thick BP sample as an example to demonstrate experimental procedures and data processing methods. Figures 2(a) and 2(b) show the optical images of the "as transferred" 157.6-nm thick sample and its "laser modified" counterpart. The uniform color of the suspended area suggests that it has a uniform thickness. The "as transferred" sample has a $22 \times 22\ \mu\text{m}^2$ suspended area, and the "laser modified" one has an $18.12 \times 22\ \mu\text{m}^2$ suspended area. The sample thickness is determined directly from the supported area, which is closely adjacent to the suspended area. Figure 2(c) shows the AFM image of the area within yellow dashed lines [Fig. 2(b)]. The height profile along the white line in the AFM image shows that the BP sample is 157.6-nm thick [Fig. 2(d)]. The FR-Raman experiment involves the measurement of two series of data: the variation of the wavenumber with the modulation frequency $\omega(f)$; the variation of the wavenumber with the CW laser power P . Sections V A and V B describe how these data are measured.

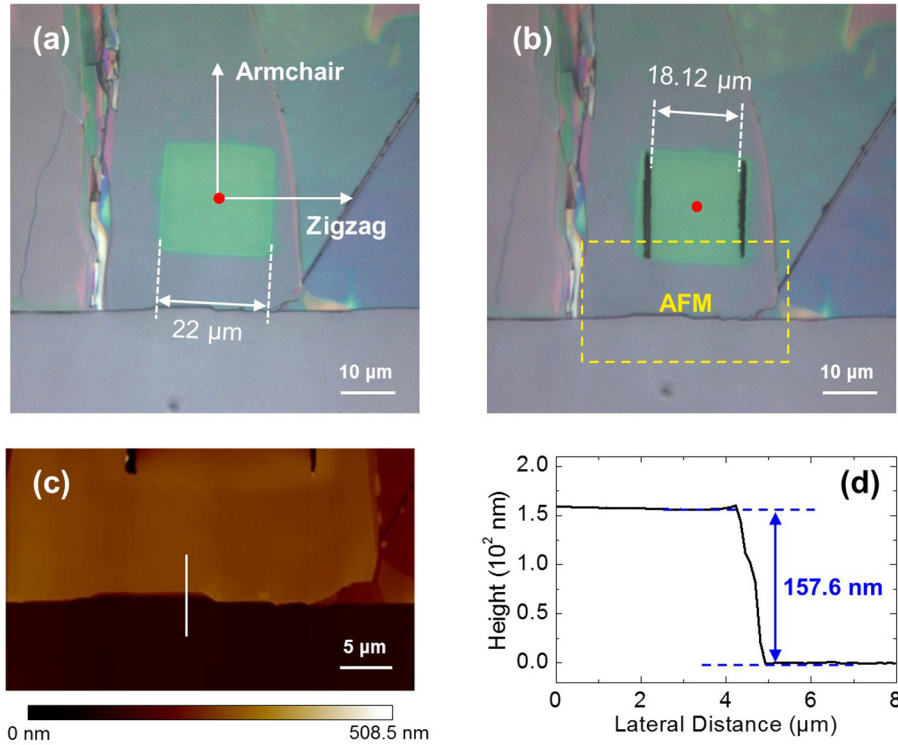


FIG. 2. (a) The optical image of the “as transferred” 157.6-nm thick sample. The armchair/zigzag direction is perpendicular/parallel to the naturally formed edge of the BP sample. The suspended area of the BP sample is $22 \times 22 \mu\text{m}^2$. The red dot marks the center of the suspended area, which is irradiated by a focused laser beam for thermal characterization. (b) The optical image of the “laser modified” 157.6-nm thick sample. Its suspended area is $18.12 \mu\text{m} \times 22 \mu\text{m}$. The red dot marks the center of the suspended area, which is irradiated by a focused laser beam for thermal characterization. The area within yellow dashed lines is thoroughly characterized by AFM. (c) The AFM image of the BP area within yellow dashed lines. The thickness of the BP sample is determined from the height profile along the white line. (d) The height profile along the white line in the AFM image. The thickness is determined as 157.6 nm.

A. Measurement of $\omega(f)$

A square-wave modulated laser at frequencies in the range of 1000 Hz to 20 MHz is used to irradiate the 157.6-nm thick sample. This modulation frequency range is broad enough to induce thermal responses from the “quasi-steady state” to the “steady state”. We take great care on selecting an appropriate laser power, so that the sample will not be damaged while sufficiently strong Raman signals can be excited. Here, we use P_m to represent the power of a modulated laser during the laser-on time. Once an appropriate P_m is selected, it is kept constant regardless of modulation frequency. The acquired Raman spectral intensity is shown by the contour map in Fig. 3(a). The most notable features of these Raman spectra are three Raman peaks A_g^1 , B_{2g} , and A_g^2 at 361, 438 and 466 cm^{-1} , respectively.^{34,35} They demonstrate strong variation in the wavenumber against f , but very weak variation in the intensity and the linewidth. Apparently, the A_g^2 mode has the largest variation in the wavenumber due to its high thermal sensitivity.¹³ Therefore, we use the A_g^2 peak wavenumber (ω) to monitor local temperature rise and extract the anisotropic thermal conductivity of BP. The A_g^2 peak wavenumber (ω) is plotted against the modulation frequency f in Fig. 3(b). As we have expected, ω increases with increased f , and it has a total variation of $\sim 1.0 \text{ cm}^{-1}$ (from ~ 464 to $\sim 465 \text{ cm}^{-1}$). The convergence of $\omega(f)$ at the high and low f is solid evidence that the transition from the “quasi-steady state” to the “steady state” does happen. $\omega(f)$ is dependent on BP’s thermal properties and the absorbed laser power. BP’s thermal properties determine how fast ω can vary from the “quasi-steady state” to the “steady state”. The absorbed laser power determines how large ω can change from the “quasi-steady state” to the “steady state”. To eliminate the influence of the absorbed laser power, we need to convert $\omega(f)$ into the

normalized average temperature rise $\bar{\theta}_{nor}$. This conversion is accomplished by using data obtained from the variation of the wavenumber with the CW laser power $\omega(P)$.

B. Measurement of $\omega(P)$

This measurement is conducted when the EOM is turned off. Therefore, a CW laser becomes the energy source. Various laser powers are applied to irradiate the “as transferred” sample. Here, we emphasize that no matter what laser powers are used, the largest one P_{max} must be equal to P_m . Considering its significant importance for the normalization, the thermal response to the CW laser with a power of P_{max} is defined as the “CW steady state”. This thermal state is indeed equivalent to the “steady state” of the modulated laser with a power of P_m . In the “CW steady state,” the wavenumber ω_s and the total variation in the wavenumber $\Delta\omega$ are crucial to convert $\omega(f)$ into $\bar{\theta}_{nor}$. ω_s is directly obtained from experimental data, while $\Delta\omega$ is calculated from $\Phi_1 \cdot P_{max}$, where Φ_1 is the change in wavenumber per unit incident laser power.

The Raman spectral intensity excited by various laser powers is shown by the contour in Fig. 3(c-1). Obviously, Raman spectra have increased intensity, red-shifted wavenumber and broadening linewidth when laser power increases. The A_g^2 mode wavenumber is plotted against laser power with red dots in Fig. 3(d). The wavenumber shows a linear dependence on laser power. The best fitting linear function to experimental data has $\Phi_1 = -0.528 \pm 0.009 \text{ cm}^{-1}/\text{mW}$. The above measurement is repeated on the “laser modified” sample with the same series of laser powers. Its result suggests that Raman spectra have increased intensity, red-shifted wavenumber and broadening linewidth with increased laser power, as shown in Fig. 3(c-2). Compared with the “as transferred” sample, the “laser modified” one has a larger change in the wavenumber.

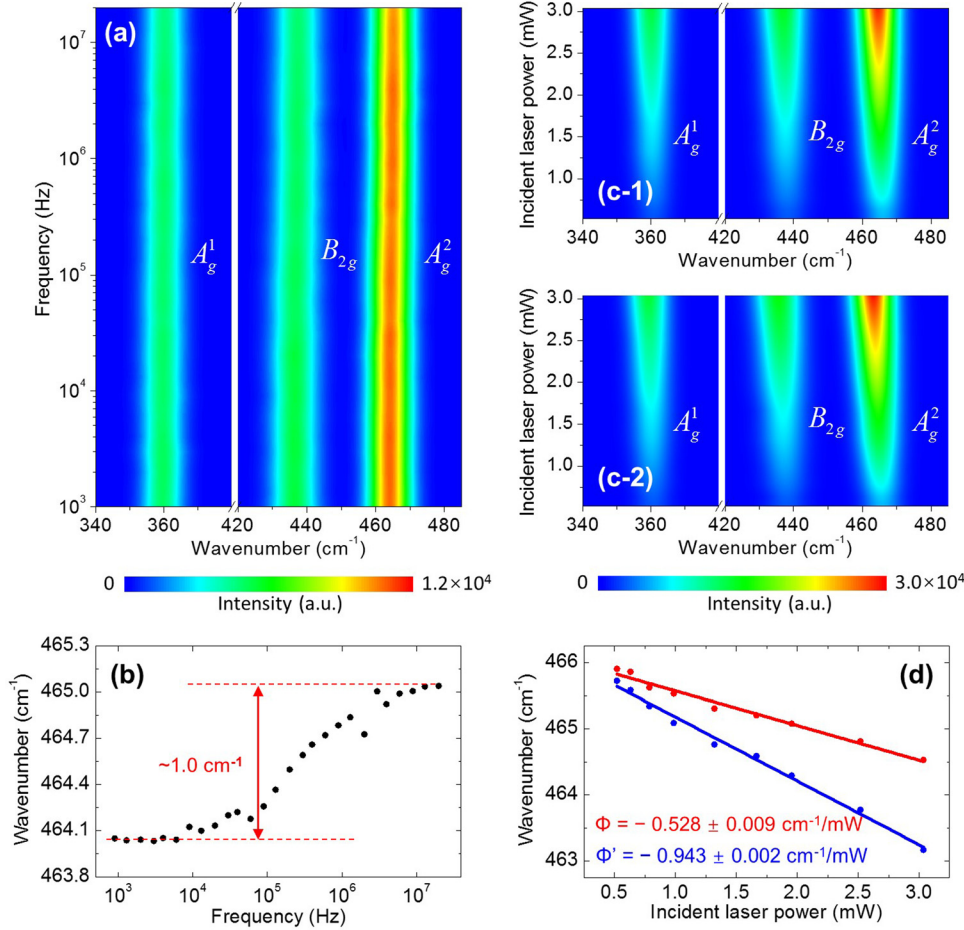


FIG. 3. (a) Raman spectral intensity of the “as transferred” 157.6-nm thick sample excited by a modulated laser with frequencies from 1000 Hz to 20 MHz. (b) The variation of the A_g^2 mode wavenumber ω with the modulation frequency f . The total variation is $\sim 1.0 \text{ cm}^{-1}$. (c) Raman spectral intensity of the “as transferred” 157.6-nm thick sample (c-1) and the “laser modified” 157.6-nm thick sample (c-2) excited by various laser powers. (d) The variation of the A_g^2 mode wavenumber with laser power. The red (blue) dots represent experimental data obtained from the “as transferred” (“as modified”) sample. The best fitting linear function to experimental data is given by a line.

The A_g^2 mode wavenumber is plotted against laser power with blue dots in Fig. 3(d). Experimental data are fitted by a linear function, which gives $\Phi_2 = -0.943 \pm 0.002 \text{ cm}^{-1}/\text{mW}$. In terms of the absolute value, Φ_2 is much larger than Φ_1 . It suggests that the average temperature rise in the “laser modified” sample is much larger than that in the “as transferred” sample. This phenomenon results from the change in thermal transport along the BP plane. For the “laser modified” sample, heat conduction to the substrate happens only in the armchair direction. So, under the same power laser heating, it will have a higher temperature rise. Φ_1 and Φ_2 are essential to determine the anisotropy of BP’s thermal conductivity.

VI. DETERMINATION OF ANISOTROPIC THERMAL CONDUCTIVITY

The complete characterization of anisotropic thermal conductivity of BP requires the determination of two parameters: the thermal conductivity ratio η (κ_{ZZ}/κ_{AC}) and the armchair thermal conductivity κ_{AC} . This section introduces how to extract η and κ_{AC} from the above experimental data.

A. Determination of η

Φ_1 and Φ_2 are two key parameters to determining η . As we have mentioned before, Φ_1 and Φ_2 are measured from the “as transferred” sample and its “laser modified” counterpart. The “as transferred” sample has four edges closely attached

to the Si wafer. The Si wafer acts as a heat sink for dissipating laser-induced heat from the center of the suspended area. The heat sink temperature remains unchanged due to the high thermal conductivity of crystal silicon.³⁶ Because the thermal conductivity of N_2 gas is negligible, laser-induced heat can only be dissipated along the BP plane.³⁶ The interfacial thermal resistance between BP and Si has negligible effect on the heat transfer, so we believe that the temperature at the margin of the suspended BP area remains unchanged despite the fact that the middle of the suspended BP area is under direct laser irradiation. In the “laser modified” sample, heat is forced to dissipate toward two paralleled edges along the armchair direction predominantly. In other words, the change in the configuration of a suspended BP sample alters thermal transport in a way that heat dissipation in the zigzag direction is suppressed significantly. This leads to a higher temperature rise in the “laser modified” sample. For a simple description, under irradiation of a unit incident laser power, the average temperature rise in the heating region of the “as transferred” sample and its “laser modified” counterpart are defined as ΔT_1 and ΔT_2 , respectively. $\Phi_1 = \chi \cdot \Delta T_1$ and $\Phi_2 = \chi \cdot \Delta T_2$, where χ is the temperature coefficient.³⁷ Hence, Φ_2/Φ_1 is equal to $\Delta T_2/\Delta T_1$. Despite Φ_2 and Φ_1 being dependent on κ_{AC} and κ_{ZZ} , their ratio Φ_2/Φ_1 is only dependent on η . The variation of $\Delta T_2/\Delta T_1$ with η can be simulated with the commercial software ANSYS. Then, by interpolating Φ_2/Φ_1 to the simulated curve of $\Delta T_2/\Delta T_1$, η can be determined at last.

Due to the fact that a suspended BP sample has a lateral size much larger than its thickness, heat conduction in the thickness direction is negligible. Thus, we can model heat conduction in a suspended BP sample with the two-dimensional heat conduction equation

$$\frac{\partial^2 T}{\partial x^2} + \eta \frac{\partial^2 T}{\partial y^2} = -\frac{\dot{Q}}{\kappa_{AC}}, \quad (1)$$

where \dot{Q} is the absorbed laser power per unit time. Solving of Eq. (1) gives the temperature rise ΔT . ΔT is a function of three unknown parameters, η , κ_{AC} and \dot{Q} . Since Eq. (1) is a linear function, we have $\Delta T \propto \dot{Q}\xi(\eta)/\kappa_{AC}$. So, $\Delta T_1 = \dot{Q}f(\eta)/\kappa_{AC}$ and $\Delta T_2 = \dot{Q}g(\eta)/\kappa_{AC}$. Then, $\Delta T_2/\Delta T_1 = g(\eta)/f(\eta)$, and we have $\Phi_2/\Phi_1 = g(\eta)/f(\eta)$. As a result, Φ_2/Φ_1 is a function of η , and it is only determined by η .

We use the commercial software ANSYS to simulate ΔT_2 and ΔT_1 separately, and then calculate their ratio $\Delta T_2/\Delta T_1$. In ANSYS simulations, since $\Delta T_2/\Delta T_1$ is not relevant to \dot{Q} and κ_{AC} , ΔT_2 and ΔT_1 can be calculated under the arbitrary setting values of \dot{Q} and κ_{AC} . For the “as transferred” sample, its boundaries are prescribed as constant temperature.³⁸ For the “laser modified” one, boundaries along the zigzag direction are prescribed as constant temperature, while boundaries along the armchair direction are prescribed as insulated.³⁸ Our numerical model strictly mimics the actual dimension of a sample. Figures 4(a) and 4(b) show simulation results of the 157.6-nm thick sample, when η is set as 3. The simulated temperature rise distribution has been normalized. They have a same heating source, which is located within a white circle. As shown in Fig. 4(a), there is radial heat flow from the heating source to borders. The shape of the heat front propagating through the BP plane is elongated in the zigzag direction due to its higher thermal conductivity. However, the normalized temperature rise distribution changed significantly in the “laser modified” sample. Due to the restricted heat conduction in the zigzag direction, heat flows with a plane wavefront in two opposite directions toward borders. Compared with the normalized temperature rise distribution in Fig. 4(a), the heating source has a much stronger heating effect. Also, the normalized temperature rise distribution extends to a much larger area outside the heating source. This phenomenon can probably result in the measurement error of η , which will be discussed in detail in Sec. VII. In these two cases of simulations, their normalized average temperature rise within white circles are

ΔT_1 and ΔT_2 , respectively. By repeating simulations with different setting values of η , we eventually have the theoretical curve of $\Delta T_2/\Delta T_1$, as shown in Fig. 4(c). For the 157.6-nm thick sample, Φ_2/Φ_1 is measured as 1.79. Then, η is determined as 3.06 by interpolation. With known η , we can continue to calculate κ_{AC} from $\omega(f)$.

B. Determination of κ_{AC}

The determination of κ_{AC} requires comparisons between the experimental normalized average temperature rise $\bar{\theta}_{nor-e}$ and its simulated counterpart $\bar{\theta}_{nor-s}$. Treated as a free parameter, κ_{AC} is determined by adjusting its value until the standard deviation between $\bar{\theta}_{nor-e}$ and $\bar{\theta}_{nor-s}$ is minimized. $\bar{\theta}_{nor-e}$ is calculated from $\omega(f)$ using the following expression:

$$\bar{\theta}_{nor-e} = 1 + [\omega(f) - \omega_s]/\Delta\omega, \quad (2)$$

where $\Delta\omega$ and ω_s are parameters obtained from the “CW steady state”. In theory, $\bar{\theta}_{nor-e}$ decreases from 1 (the “steady state”) to 0.5 (the “quasi-steady state”) with increased f . However, in actual cases, measurement errors of $\Delta\omega$ and ω_s lead to the deviation of $\bar{\theta}_{nor-e}$ more or less. Here, we use a factor C to correct $\bar{\theta}_{nor-e}$. The corrected $\bar{\theta}_{nor-e}$ has an expression of

$$\bar{\theta}_{nor-e} = 1 + C \cdot [\omega(f) - \omega_s]/\Delta\omega. \quad (3)$$

After the correction with parameter C , $\bar{\theta}_{nor-e}$ is guaranteed to vary from 0.5 to 1 with increased f . The correction leads to an improved fitting result. The measurement error induced by the correction will be discussed in Sec. VII. For the 157.6-nm thick sample, it is $\bar{\theta}_{nor-e}$ after the correction is plotted with black dots in Fig. 5(a). These experimental data are the average of 10 measurements. Their error bars are the standard deviation of 10 measurements. At high frequencies, experimental data have a relatively larger standard deviation, which is relevant to the deformation of the modulated laser waveform.

The calculation of $\bar{\theta}_{nor-s}$ requires simulations of thermal responses to a modulated laser. However, such simulations are complicated and very time-consuming even with the help of ANSYS. Therefore, a semi-analytical method is developed to simplify and expedite simulations. This method takes advantage of ANSYS to simulate the thermal response to a step-laser first. Then, based on the temperature linear response and the superposition law, the thermal response to a

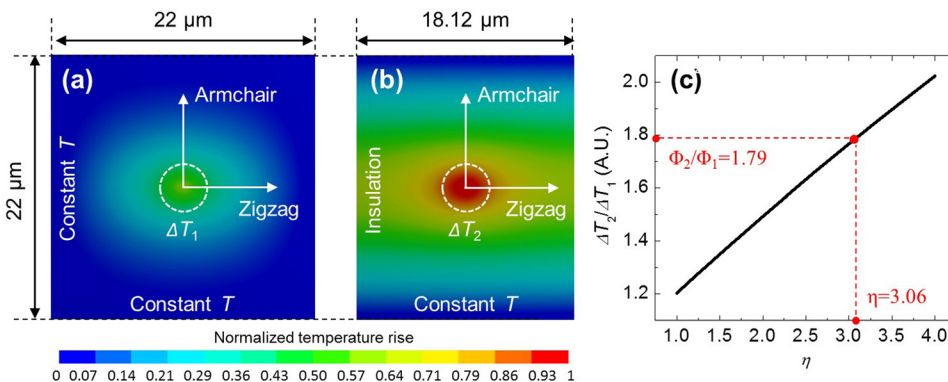


FIG. 4. Simulated normalized temperature rise distribution in the “as transferred” 157.6-nm thick sample (a) and the “laser modified” 157.6-nm thick sample (b). White circles give the range of a heating source. (c) The theoretical curve of $\Delta T_2/\Delta T_1$ as a function of η . By interpolating $\Phi_2/\Phi_1=1.79$ to the theoretical curve, η of the 157.6-nm thick sample is determined as 3.06.

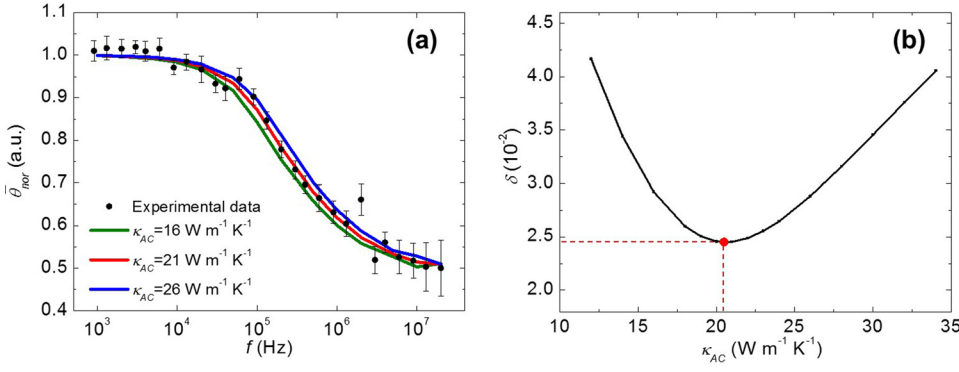


FIG. 5. (a) The fitting of experimental data by various theoretical curves. Experimental data are plotted with black dots. Their error bars represent the standard deviation. The best fitting curve is plotted with red color. Its κ_{AC} is equal to $21 \text{ W m}^{-1} \text{ K}^{-1}$. The green and blue curves are calculated with $\kappa_{AC} = 16$ and $\kappa_{AC} = 26 \text{ W m}^{-1} \text{ K}^{-1}$, respectively. (b) The standard deviation δ of experimental data to theoretical curves as a function of κ_{AC} . The red dot shows the smallest δ . Its corresponding κ_{AC} is $21 \text{ W m}^{-1} \text{ K}^{-1}$.

modulated laser can be constructed from the thermal response to a step-wave laser. Modeled with the two-dimensional thermal transport in ANSYS, the thermal response to a step-laser is represented by $\theta_s(t)$. $\theta_s(t)$ represents the temperature rise as a function of time. Therefore, the thermal response to a modulated laser with a frequency f is given by

$$\theta_m(t_p) = \sum_{n=0}^{\infty} (-1)^n \cdot \theta_s(t_p + n \cdot \tau_h), \quad (4)$$

where τ_h (laser-on time) is equal to $1/(2f)$.²⁸ $\theta_m(t_p)$ gives the evolution of temperature rise in a steady periodic thermal state during τ_h . Its corresponding average temperature rise during τ_h is given by

$$\bar{\theta}_m = \frac{\int_0^{\tau_h} \theta_m(t_p) dt}{\tau_h}. \quad (5)$$

When τ_h is infinitely large, we have $\bar{\theta}_{\infty}$, which is the average temperature rise in the “steady state”. Normalizing $\bar{\theta}_m$ with $\bar{\theta}_{\infty}$, we have the simulated normalized average temperature rise $\bar{\theta}_{nor-s}$ which is equal to

$$\bar{\theta}_{nor-s} = \frac{\int_0^{\tau_h} \theta_m(t_p) dt}{\tau_h \cdot \bar{\theta}_{\infty}}. \quad (6)$$

$\bar{\theta}_{nor-s}$ is a function of f and κ_{AC} . The variation of $\bar{\theta}_{nor-s}$ with f is only determined by κ_{AC} since we already know η . By calculating the variation of $\bar{\theta}_{nor-s}$ with f at various trial values of κ_{AC} , we can obtain theoretical curves for fitting experimental data.

Three theoretical curves of the 157.6-nm thick sample are plotted in Fig. 5(a). The red one is the best fitting curve to $\bar{\theta}_{nor-s}$ with κ_{AC} equal to $21 \text{ W m}^{-1} \text{ K}^{-1}$. The green and blue curves are calculated, when κ_{AC} are equal to 16 and $26 \text{ W m}^{-1} \text{ K}^{-1}$, respectively. The best fitting curve has the smallest standard deviation δ , which is identified from the parabolic-like κ_{AC} - δ curve [Fig. 5(b)]. The smallest δ has been marked with a red dot in Fig. 5(b).

VII. MEASUREMENT RESULTS AND DISCUSSION

In total, four samples with thicknesses of 99.8, 112.3, 145.9 and 157.6 nm are successfully prepared and studied. Measurement results are listed in Table I. It can be found

that $\kappa_{AC} = 14$ – 22 and $\kappa_{ZZ} = 40$ – $63 \text{ W m}^{-1} \text{ K}^{-1}$. They are comparable to these results obtained by micro-Raman spectroscopy ($\kappa_{AC} = \sim 20$ and $\kappa_{ZZ} = \sim 40 \text{ W m}^{-1} \text{ K}^{-1}$),¹³ TDTR technique ($\kappa_{AC} = 26$ – 34 and $\kappa_{ZZ} = 62$ – $86 \text{ W m}^{-1} \text{ K}^{-1}$ by Jang *et al.*, and $\kappa_{AC} = 23$ – 33 and $\kappa_{ZZ} = 73$ – $93 \text{ W m}^{-1} \text{ K}^{-1}$ by Sun *et al.*),^{14,16} and micro-bridge technique (κ_{AC} decreases from ~ 15 to $\sim 5 \text{ W m}^{-1} \text{ K}^{-1}$, and κ_{ZZ} decreases from ~ 27 to $\sim 12 \text{ W m}^{-1} \text{ K}^{-1}$ as the thickness varies from ~ 300 to $\sim 50 \text{ nm}$).¹⁷ The discrepancy of these experimental measurements is relevant to the methods used for sample preparation, data processing and thermal transport modeling. Our measured results have demonstrated large measurement errors. Two common effects, the thickness effect and the oxidation effect, are not responsible for data deviation in our work. Previous research has concluded that in-plane thermal conductivity increases with increased thickness in BP due to strong surface scattering.³⁹ The thickness effect is excluded by our observed irregular dependence of κ_{AC} and κ_{ZZ} on the thickness. Meanwhile, the oxidation effect is negligible since our BP samples are protected well by dry N_2 gas.^{40,41} So far, we believe that measurement errors originate from factors, such as the gravity-induced deformation, the existence of micro-wrinkles/micro-bubbles, the temperature dependence of BP’s physical properties, and the correction of normalized data. Here, we study measurement errors by analyzing η and κ_{AC} , which are two independent parameters (κ_{ZZ} is calculated as $\kappa_{ZZ} = \eta \cdot \kappa_{AC}$).

In the ANSYS simulation model, we assume that the supported area of BP contacts perfectly with the Si substrate and the suspended area of BP is completely flat. However, these assumptions are challenged by facts that micro-wrinkles/micro-bubbles exist between the supported area of BP and the Si substrate, and the suspended area of BP is deformed under the force of gravity.^{18,42–44} The existence of micro-wrinkles/micro-bubbles makes it inaccurate to

TABLE I. Experimental results of 99.8, 112.3, 145.9, and 157.6-nm thick suspended BP samples. η and κ_{AC} are extracted from experimental data. κ_{ZZ} is calculated from η and κ_{AC} .

Thickness (nm)	η	κ_{AC} ($\text{W m}^{-1} \text{ K}^{-1}$)	κ_{ZZ} ($\text{W m}^{-1} \text{ K}^{-1}$)
99.8	2.64	21	55
112.3	1.86	22	41
145.9	2.95	14	40
157.6	3.06	21	63

describe the boundaries of suspended area with constant temperature in the thermal transport model. With a large suspended area, the gravity-induced deformation is inevitable. For an “as transferred” sample and its “laser modified” counterpart, their suspended area is at different states of force balance. Typically, the suspended area of a “laser modified” sample has larger deformation than that of an “as transferred” sample. The deformation has two effects: the area under direct irradiation of a laser beam is larger than the laser spot size and the actual suspended area is relatively larger than it should be. The micro-wrinkles/micro-bubbles and deformation are morphological features closely related to the characteristic of each sample. As a result, measurement errors of η and κ_{AC} are related to sample characteristics.

The temperature dependence of BP’s physical properties also contributes to large measurement errors of η . As shown in Figs. 4(a) and 4(b), compared with the “as transferred” sample, the “laser modified” one has a higher normalized temperature rise and a larger normalized temperature rise distribution. The physical properties of these two samples are under the influence of temperature. Apparently, the physical properties of the “laser modified” sample are under a larger influence of temperature. However, in ANSYS simulations, we do not consider the temperature dependence of BP’s physical properties, and simply use their values at 300 K to conduct numerical calculations. Such mismatch in the model and actual conditions leads to measurement errors of η . The degree of influence of the mismatch on the determination of η is sample-dependent, since appropriate laser powers applied to conduct an experiment are sample-dependent. Combined with the deformation and micro-wrinkles/micro-bubbles, they lead to large measurement errors of η .

The correction of normalized data $\bar{\theta}_{nor-e}$ plays another important role in the measurement errors of κ_{AC} . Since a theoretical curve $\bar{\theta}_{nor-s}$ is not very sensitive to the change in κ_{AC} , even a minor correction of $\bar{\theta}_{nor-e}$ can lead to large measurement errors. The ideal $\bar{\theta}_{nor-e}$ varies from 1 to 0.5 with increased f . However, in actual cases, $\bar{\theta}_{nor-e}$ without a correction varies from 1 to a value slightly larger or smaller than 0.5 due to the relatively larger standard deviation at high frequencies, as shown in Fig. 5(a). Under the correction with parameter C , the distribution of $\bar{\theta}_{nor-e}$ is stretched downward/upward to 0.5, which will give a lower/higher κ_{AC} . Obviously, $\bar{\theta}_{nor-e}$ requiring little or no correction can generate a more accurate κ_{AC} . So, the measurement accuracy is fully determined by the quality of experimental data $\bar{\theta}_{nor-e}$. For example, the 145.9-nm sample has $\kappa_{ac} = 14 \text{ W m}^{-1} \text{ K}^{-1}$, which deviates from the rest severely. This large deviation in κ_{AC} is indeed a result of the abnormal low quality of experimental data. The data quality is a result of the interaction of many factors, such as the gravity-induced deformation, the existence of micro-wrinkles/micro-bubbles, the temperature dependence of BP’s physical properties, as well as operation skills of researchers. However, how these factors influence the data quality is not yet fully understood, and more work is required to figure it out in future.

Based on the above analysis, we have developed useful strategies to optimize the FR-Raman technique by suppressing measurement errors. For example, we can reduce the

gravity-induced deformation by suspending a BP sample on a smaller square dent. Also, we can improve the modeling accuracy by considering the variation of BP’s physical properties with temperature in our thermal transport model. However, the modeling accuracy is improved at the expense of the simulation efficiency. So, how to balance the modeling accuracy and the simulation efficiency is a topic we should consider seriously in future work. Moreover, we can choose a laser with a longer wavelength as an energy source. A laser with a longer wavelength, e.g., 633 nm, is good for providing a clear and strong Raman spectrum but does not produce local heating as much as our current 532 nm laser.⁴⁵ Consequently, the signal-to-noise ratio of a Raman spectrum can be improved, and the fitting error of $\bar{\theta}_{nor-e}$ can be reduced. We believe that these strategies can improve the measurement accuracy of the FR-Raman technique and lay a foundation for its wide application in the future.

VIII. CONCLUSION

In summary, we have successfully applied the FR-Raman technique to measure the anisotropic thermal conductivities of BP. By using CW laser heating and Raman measurement of BP samples of both armchair/zigzag and only armchair heat conduction, the thermal conductivity ratio η (κ_{ZZ}/κ_{AC}) is found to be between 1.86 and 3.06. κ_{AC} is $\sim 21 \text{ W m}^{-1} \text{ K}^{-1}$ except for the 145.9-nm thick sample. κ_{ZZ} is between 40 and 63 $\text{W m}^{-1} \text{ K}^{-1}$. By analyzing experimental procedures and data processing methods carefully, we have identified several reasons responsible for the large measurement uncertainties. This study significantly extends the application of the FR-Raman technique to nm-thick suspended two-dimensional atomic layer materials. This study not only lays the foundation for the wide application of FR-Raman technique for nondestructive thermal characterization, but also advances our fundamental understanding of the anisotropic phonon transport in BP.

ACKNOWLEDGMENTS

Support of this work by National Science Foundation (CBET1235852 and CMMI1264399), Department of Energy (DENE0000671 and DEEE0007686), and Iowa Energy Center (MG-16-025 and OG-17-005) is gratefully acknowledged.

¹L. K. Li, Y. J. Yu, G. J. Ye, Q. Q. Ge, X. D. Ou, H. Wu, D. L. Feng, X. H. Chen, and Y. B. Zhang, *Nat. Nanotechnol.* **9**, 372 (2014).

²J. S. Qiao, X. H. Kong, Z. X. Hu, F. Yang, and W. Ji, *Nat. Commun.* **5**, 4475 (2014).

³F. N. Xia, H. Wang, and Y. C. Jia, *Nat. Commun.* **5**, 4458 (2014).

⁴H. Liu, A. T. Neal, Z. Zhu, Z. Luo, X. F. Xu, D. Tomanek, and P. D. D. Ye, *ACS Nano* **8**, 4033 (2014).

⁵R. X. Fei and L. Yang, *Nano Lett.* **14**, 2884 (2014).

⁶X. M. Wang, A. M. Jones, K. L. Seyler, V. Tran, Y. C. Jia, H. Zhao, H. Wang, L. Yang, X. D. Xu, and F. N. Xia, *Nat. Nanotechnol.* **10**, 517 (2015).

⁷X. Ling, S. X. Huang, E. H. Hasdeo, L. B. Liang, W. M. Parkin, Y. Tatsumi, A. R. T. Nugraha, A. A. Puzos, P. M. Das, B. G. Sumpter, D. B. Geohegan, J. Kong, R. Saito, M. Drndic, V. Meunier, and M. S. Dresselhaus, *Nano Lett.* **16**, 2260 (2016).

- ⁸N. N. Mao, J. Y. Tang, L. M. Xie, J. X. Wu, B. W. Han, J. J. Lin, S. B. Deng, W. Ji, H. Xu, K. H. Liu, L. M. Tong, and J. Zhang, *J. Am. Chem. Soc.* **138**, 300 (2016).
- ⁹H. Chen, P. Huang, D. Guo, and G. X. Xie, *J. Phys. Chem. C* **120**, 29491 (2016).
- ¹⁰H. Y. Sun, G. Liu, Q. F. Li, and X. G. Wan, *Phys. Lett. A* **380**, 2098 (2016).
- ¹¹J. W. Jiang and H. S. Park, *J. Phys. D: Appl. Phys.* **47**, 385304 (2014).
- ¹²Q. Wei and X. H. Peng, *Appl. Phys. Lett.* **104**, 251915 (2014).
- ¹³Z. Luo, J. Maassen, Y. X. Deng, Y. C. Du, R. P. Garrelts, M. S. Lundstrom, P. D. Ye, and X. F. Xu, *Nat. Commun.* **6**, 8572 (2015).
- ¹⁴H. J. Jang, J. D. Wood, C. R. Ryder, M. C. Hersam, and D. G. Cahill, *Adv. Mater.* **27**, 8017 (2015).
- ¹⁵Y. Wang, G. Z. Xu, Z. P. Hou, B. C. Yang, X. M. Zhang, E. K. Liu, X. K. Xi, Z. Y. Liu, Z. M. Zeng, W. H. Wang, and G. H. Wu, *Appl. Phys. Lett.* **108**, 092102 (2016).
- ¹⁶B. Sun, X. Gu, Q. Zeng, X. Huang, Y. Yan, Z. Liu, R. Yang, and Y. K. Koh, *Adv. Mater.* **29**, 1603297 (2017).
- ¹⁷S. Lee, F. Yang, J. Suh, S. J. Yang, Y. Lee, G. Li, H. S. Choe, A. Suslu, Y. B. Chen, C. Ko, J. Park, K. Liu, J. B. Li, K. Hippalgaonkar, J. J. Urban, S. Tongay, and J. Q. Wu, *Nat. Commun.* **6**, 8573 (2015).
- ¹⁸T. Wang, R. Wang, P. Yuan, S. Xu, J. Liu, and X. Wang, *Adv. Mater. Interfaces* **4**, 1700233 (2017).
- ¹⁹A. Tiwari, K. Boussois, B. Nait-Ali, D. S. Smith, and P. Blanchart, *AIIP Adv.* **3**, 112129 (2013).
- ²⁰M. Han, J. Liu, Y. S. Xie, and X. W. Wang, *Carbon* **126**, 532 (2018).
- ²¹J. Liu, T. Y. Wang, S. Xu, P. Y. Yuan, X. Xu, and X. W. Wang, *Nanoscale* **8**, 10298 (2016).
- ²²Y. S. Xie, P. Y. Yuan, T. Y. Wang, N. Hashemi, and X. W. Wang, *Nanoscale* **8**, 17581 (2016).
- ²³B. W. Zhu, J. Liu, T. Y. Wang, M. Han, S. Valloppilly, S. Xu, and X. W. Wang, *ACS Omega* **2**, 3931 (2017).
- ²⁴J. Liu, W. D. Qu, Y. S. Xie, B. W. Zhu, T. Y. Wang, X. L. Bai, and X. W. Wang, *Carbon* **121**, 35 (2017).
- ²⁵P. Yuan, C. Li, S. Xu, J. Liu, and X. Wang, *Acta Mater.* **122**, 152 (2017).
- ²⁶X. D. Tang, S. Xu, J. C. Zhang, and X. W. Wang, *ACS Appl. Mater. Interfaces* **6**, 2809 (2014).
- ²⁷X. D. Tang, S. Xu, and X. W. Wang, *Nanoscale* **6**, 8822 (2014).
- ²⁸T. Y. Wang, S. Xu, D. H. Hurley, Y. N. Yue, and X. W. Wang, *Opt. Lett.* **41**, 80 (2016).
- ²⁹T. Wang, J. Liu, B. Xu, R. Wang, P. Yuan, M. Han, S. Xu, Y. Xie, Y. Wu, and X. Wang, *ChemPhysChem* **18**, 2828 (2017).
- ³⁰M. Xu, T. Liang, M. Shi, and H. Chen, *Chem. Rev.* **113**, 3766 (2013).
- ³¹A. Castellanos-Gomez, M. Buscema, R. Molenaar, V. Singh, L. Janssen, H. S. J. van der Zant, and G. A. Steele, *2D Mater.* **1**, 011002 (2014).
- ³²A. Castellanos-Gomez, L. Vicarelli, E. Prada, J. O. Island, K. Narasimha-Acharya, S. I. Blanter, D. J. Groenendijk, M. Buscema, G. A. Steele, and J. Alvarez, *2D Mater.* **1**, 025001 (2014).
- ³³J. Kim, J. U. Lee, J. Lee, H. J. Park, Z. Lee, C. Lee, and H. Cheong, *Nanoscale* **7**, 18708 (2015).
- ³⁴D. J. Late, *ACS Appl. Mater. Interfaces* **7**, 5857 (2015).
- ³⁵A. Lapinska, A. Taube, J. Judek, and M. Zdrojek, *J. Phys. Chem. C* **120**, 5265 (2016).
- ³⁶T. L. Bergman, F. P. Incropera, D. P. DeWitt, and A. S. Lavine, *Fundamentals of Heat and Mass Transfer* (John Wiley and Sons, 2011).
- ³⁷I. Calizo, A. A. Balandin, W. Bao, F. Miao, and C. N. Lau, *Nano Lett.* **7**, 2645 (2007).
- ³⁸S. Subrina and D. Kotchetkov, *J. Nanoelectron. Optoelectron.* **3**, 249 (2008).
- ³⁹Y. X. Wang, N. Xu, D. Y. Li, and J. Zhu, *Adv. Funct. Mater.* **27**, 1604134 (2017).
- ⁴⁰J. D. Wood, S. A. Wells, D. Jariwala, K. S. Chen, E. Cho, V. K. Sangwan, X. L. Liu, L. J. Lauhon, T. J. Marks, and M. C. Hersam, *Nano Lett.* **14**, 6964 (2014).
- ⁴¹X. L. Liu, J. D. Wood, K. S. Chen, E. Cho, and M. C. Hersam, *J. Phys. Chem. Lett.* **6**, 773 (2015).
- ⁴²D. Yoon, Y. W. Son, and H. Cheong, *Nano Lett.* **11**, 3227 (2011).
- ⁴³L. Q. Su, Y. Zhang, Y. F. Yu, and L. Y. Cao, *Nanoscale* **6**, 4920 (2014).
- ⁴⁴B. Huang and Y. K. Koh, *Carbon* **105**, 268 (2016).
- ⁴⁵A. A. Balandin, S. Ghosh, W. Z. Bao, I. Calizo, D. Teweldebrhan, F. Miao, and C. N. Lau, *Nano Lett.* **8**, 902 (2008).